Mineralogical Magazine (2023), **87**, 542–553
doi:10.1180/mgm.2023.31

CAMBRIDGE UNIVERSITY PRESS

Article

High-temperature behaviour of fedorite, $Na_{2.5}(Ca_{4.5}Na_{2.5})[Si_{16}O_{38}]F_2{\cdot}2.8H_2O$, from the Murun Alkaline Complex, Russia

Maria Lacalamita[1], Ernesto Mesto[1], Ekaterina Kaneva[2,3], Roman Shendrik[2], Tatiana Radomskaya[2,3] and Emanuela Schingaro[1]

[1]Earth and Geoenvironmental Sciences Department, University of Bari Aldo Moro, via E. Orabona 4, I-70125 Bari, Italy; [2]Vinogradov Institute of Geochemistry, Siberian Branch of the Russian Academy of Sciences, 1a Favorsky Str., 664033 Irkutsk, Russia; and [3]Sidorov Mineralogical Museum, Irkutsk National Research Technical University, 83 Lermontov Str., 664074 Irkutsk, Russia

Abstract

The thermal behaviour of fedorite from the Murun massif, Russia, has been investigated by means of electron probe microanalysis (EPMA), differential thermal analysis (DTA), thermogravimetry (TG), *in situ* high-temperature single-crystal X-ray diffraction (HT-SCXRD), *ex situ* high-temperature Fourier-transform infrared spectroscopy (HT-FTIR). The empirical chemical formula of the sample of fedorite studied is: $(Na_{1.56}K_{0.72}Sr_{0.12})_{\Sigma 2.40}(Ca_{4.42}Na_{2.54}Mn_{0.02}Fe_{0.01}Mg_{0.01})_{\Sigma 7.00}(Si_{15.98}Al_{0.02})_{\Sigma 16.00}(F_{1.92}Cl_{0.09})_{\Sigma 2.01}(O_{37.93}OH_{0.07})_{\Sigma 38.00}{\cdot}2.8H_2O$. The TG curve provides a total mass decrease of ~5.5%, associated with dehydration and defluorination processes from 25 to 1050°C. Fedorite crystallises in space group $P\bar{1}$ and has: $a = 9.6458(2)$, $b = 9.6521(2)$, $c = 12.6202(4)$ Å, $\alpha = 102.458(2)$, $\beta = 96.2250(10)$, $\gamma = 119.9020(10)°$ and cell volume, $V = 961.69(5)$ Å^3. The HT-SCXRD was carried out in air in the 25–600°C range. Overall, a continuous expansion of the unit-cell volume was observed although the *c* cell dimension slightly decreases in the explored temperature range. Structure refinements indicated that the mineral undergoes a dehydration process with the loss of most of the interlayer H_2O from 25 to 300°C. The HT-FTIR spectra confirmed that fedorite progressively dehydrates until 700°C.

Keywords: fedorite, non-ambient, *in situ* HT-SCXRD, *ex situ* HT-FTIR

(Received 1 December 2022; accepted 20 April 2023; Accepted Manuscript published online: 11 May 2023; Associate Editor: Ferdinando Bosi)

Introduction

Fedorite is a rare mineral occurring in alkaline rocks of Turiy and Murun complexes, Russia (Kukharenko *et al.*, 1965; Konev *et al.*, 1993, 1996) with formula $(K,Na)_{2.5}(Ca,Na)_7Si_{16}O_{38}(OH,F)_2{\cdot}3.5H_2O$ according to the official International Mineralogical Association Commission on New Minerals, Nomenclature and Classification (IMA–CNMNC) List of Mineral Names (Pasero, 2023).

The empirical formula of fedorite was first given by Kukharenko *et al.* (1965) as $K_{0.27}(Ca_{1.02}Na_{0.93})(Al_{0.20}Si_{3.80})O_{9.05}(OH)_{0.95}{\cdot}1.5H_2O$. Other formulae were subsequently given by several authors (Sokolova *et al.*, 1983; Joswig *et al.*, 1988; Blackburn and Dennen, 1997; Mitchell and Burns, 2001; Kaneva *et al.*, 2020a). In particular, Mitchell and Burns (2001) revised the fedorite chemical formula as $Na_3(Ca_4Na_3)[Si_{16}O_{38}]F_2{\cdot}3.5H_2O$ (as cited in Hawthorne *et al.*, 2019). More recently, Kaneva *et al.* (2020a) reported more complex formulae on fedorite from three Russian localities, with a range of values for H_2O as well as different content and possibly different structural roles for the OH groups. It is thus apparent that there are still open questions about the actual definition of fedorite.

From a structural viewpoint, this mineral has been included in the group of silicates with stacked modules consisting of sheets of tetrahedra and octahedra (Ferraris, 1997; Ferraris and Gula, 2005; Rastsvetaeva and Aksenov, 2011) and is considered as belonging to the reyerite–gyrolite group (Bonaccorsi and Merlino, 2005). Hawthorne *et al.* (2019) described fedorite as a double-layer sheet silicate based on an upper 3-connected net (6^3) with an arrangement of upward-pointing tetrahedra (u) and downward-pointing tetrahedra (d) showing $(d^6)_1(d^2ud^2u)_3$ configuration and 1:2.38 T:O ratio. The fedorite interstitial complex consists of one MO_6^{2-}, two $MO_5^{2-}F^-$ and one $MO_4^{2-}F^{2-}$ octahedra with $M = Ca^{2+}$ and Na^+ and additional disordered sites occupied by Na^+ and K^+ cations coordinated by O^{2-} and partly disordered H_2O.

The crystal structure of fedorite was solved by Sokolova *et al.* (1983) and then refined by a number of authors (Joswig *et al.*, 1988; Mitchell and Burns, 2001; Kaneva *et al.*, 2020a; this work). It consists of 4 octahedral independent sites (*M* sites), 8 tetrahedral sites (*T* sites), 19 oxygen sites, one F site and a variable number of large disordered sites (labelled *A* or *K* sites) as well as sites occupied by oxygens of H_2O (labelled *W* or Ow sites). Previous structure refinements report difficulties in modelling the position and disorder of interlayer cations and H_2O. For example, Joswig *et al.* (1988) found elongated displacement

Corresponding author: Ernesto Mesto; Email: ernesto.mesto@uniba.it
Cite this article: Lacalamita M., Mesto E., Kaneva E., Shendrik R., Radomskaya T. and Schingaro E. (2023) High-temperature behaviour of fedorite, $Na_{2.5}(Ca_{4.5}Na_{2.5})[Si_{16}O_{38}]F_2{\cdot}2.8H_2O$, from the Murun Alkaline Complex, Russia. *Mineralogical Magazine* **87**, 542–553. https://doi.org/10.1180/mgm.2023.31

ellipsoids for one of the two interlayer cations occupying the *A*1 and *A*2 sites. These sites were split into *A*1 and *A*1*a* and also into *A*2 and *A*2*a* in the structure refinement of the Turiy and Murun fedorite, respectively (Mitchell and Burns, 2001). Other problems were reported by the latter authors (correlations between site occupancy factors and displacement parameters for one of the three H_2O sites, labelled *W*3; short distance between *W*3 and *A*1*a* sites; and short distance between *A*1*a* and *A*2 sites) and different explanations were given (*W*3 locally vacant when *A*1*a* is occupied; *A*2 locally vacant when *A*1*a* is occupied; *A*2 containing H_2O if locally occupied). Kaneva *et al.* (2020a) associated elongated displacement parameters for interlayer cations and oxygen of the H_2O with mixed cationic–anionic sites occupancy in fedorite from three districts of the Murun complex. In particular, four K-occupied interlayer sites (*K*1 to *K*4) were identified: one (*K*2) or more of them (*K*2 to *K*4) were split into two or three new positions. From one (O20w) to four (O20w to O24w) H_2O were also identified by those authors.

The hydration degree of the alkaline cations in the interlayer of sheet silicate phases may strongly affect their chemical and physical properties, especially in relation to temperature changes. Specifically, the dehydration process of fedorite has not been previously explored.

In the present study, data from *in situ* high-temperature single-crystal X-ray diffraction (HT-SCXRD) as well as *ex situ* high-temperature Fourier-transform infrared spectroscopy (HT-FTIR) experiments of fedorite are provided. Results from electron probe microanalysis (EPMA), differential thermal analysis (DTA), thermogravimetry (TG) and derivative thermogravimetry (DTG) are also reported. This work follows other papers aimed at gaining insights on the crystal chemistry (Kaneva *et al.*, 2014, 2018, 2020b, 2021, 2022, 2023a, 2023b; Mesto *et al.*, 2014; Lacalamita *et al.*, 2017; Schingaro *et al.*, 2017; Lacalamita, 2018; Bogdanov *et al.*, 2021; Kaneva and Shendrik, 2022) as well as on the structural modifications of some rare minerals from Russian alkaline rocks under non-ambient conditions (Schingaro *et al.*, 2018; Comboni *et al.*, 2019; Lacalamita *et al.*, 2019).

Geological background and sample description

The geological context of Malyy Murun massif (Murun alkaline complex located in the NW Aldan Shield, Siberia, Russia, dated 137–128 Ma) is reported elsewhere (Vladykin, 2009; Vladykin *et al.*, 2018; Borovikov *et al.*, 2018) and is only briefly summarised here. The Murun massif geological history is characterised by four igneous phases or stages (early intrusive, main intrusive, volcanic and late intrusive) as well as by hydrothermal activity represented by quartz veins with rutile–brookite–anatase mineralisation (Ivanov *et al.*, 2018).

According to Kaneva *et al.* (2020a), fedorite has been found in different districts of the Murun massif: the Gavrilovskaya zone, the Irkutskiy and Yakutskiy districts. Fedorite from the Gavrilovskaya zone was found in brookite–anatase–quartz–feldspar rocks whereas fedorite from Irkutskiy and Yakutskiy districts is associated with charoite mineralisation. Mineral associations are as follow: aegirine–apatite–rutile–fedorite–pyrite–galena–quartz (Gavrilovskaya zone); apatite–fedorite–microcline–steacyite–quartz–charoite (Yakutskiy district); aegirine–tinaksite–galena–copper–fedorite–microcline–steacyite–quartz–charoite (Irkutskiy district). Melt and fluid-inclusion studies have shown that low temperature of formation occurred for mineral assemblages of brookite–anatase–feldspar–quartz rocks (from 210 to 280°C) with respect to those from charoite rocks (>800°C for early stage and 450 to 600°C for final stages of crystallisation). Kaneva *et al.* (2020a) concluded that fedorite from the Gavrilovskaya was formed at a lower temperature with respect to fedorite of the other districts, as also testified by the larger amount of H_2O found in the crystal structure of their sample Gav-43.

The fedorite-bearing sample of the present work is labelled Gav-33 (Fig. S1, in Supplementary material – see below) and was taken from brookite–quartz–feldspar rocks of the Gavrilovskaya zone (same locality as sample Gav-43 from Kaneva *et al.*, 2020a). The zone is situated at the watershed of the Davan and Atbastakh Rivers, Irkutsk region, Bodaibo district (58°19'51"N, 119°5'45"E).

The host rock has a holocrystalline coarse- and medium-grained structure and uniform texture (massive). In the thin section, the sample mainly consists of fedorite (92 vol.%), with minor components such as quartz (5 vol.%), microcline (<1 vol.%), aegirine (<1 vol.%), amphibole (<1 vol.%), calcite (<1 vol.%), pectolite (<1 vol.%); accessory minerals are apatite and rutile (Fig. S2).

The sequence of mineral crystallisation in the Gav-33 sample from early to late is: aegirine, apatite, amphibole, fedorite, microcline, rutile, quartz, pectolite and calcite (Table S1).

Experimental

Chemical analysis

A fedorite single crystal was embedded in epoxy resin, polished and carbon coated before carrying out electron probe microanalysis. A JEOL JXA-8200 electron microprobe in full wavelength dispersive spectrometry mode was used. Operating conditions were: 15 kV accelerating voltage, 5 nA sample current, ~1 mm spot size and 40 s counting time. The standards used were: grossular (Si, Al and Ca); omphacite (Na); olivine (Mg); K-feldspar (K); rhodonite (Mn); fayalite (Fe); celestine (Sr); sanbornite (Ba); scapolite (Cl) and hornblende (F).

A Phi-Rho-Z routine (Pouchou and Pichoir, 1985) was employed for the conversion from X-ray counts to oxide weight percentages (wt.%).

Thermal analysis

Simultaneous differential thermal, thermogravimetric and derivative thermogravimetric analysis (DTA/TG/DTG) were carried out with a Seiko SSC 5200 thermal analyser equipped with an ESS GeneSys Quadstar 422 quadrupole mass spectrometer which allowed the analysis of gases evolved during thermal processes. The measurements were performed both in air at a heating rate of 10°C/min in the temperature range 25–1075°C and in ultrapure He at 20°C/min in the heating range 25–1100°C. Mass analyses were done in multiple ion detection mode measuring the m/z ratios (ratio between the mass number and the charge of an ion) 17 to 20 for H_2O/HOD/D_2O isotopes and 19 for F.

X-ray diffraction analysis

Single crystals of fedorite were selected under an optical microscope and glued on the tip of a glass fibre. The crystal (0.60 × 0.59 × 0.05 mm) with the best diffraction behaviour was used

https://doi.org/10.1180/mgm.2023.31 Published online by Cambridge University Press

for the *in situ* high-temperature X-ray diffraction experiment by means of a Bruker AXS APEX II diffractometer equipped with Mo*K*α radiation (λ = 0.71073 Å) and a CCD area detector. The measurements were carried out in air from 25 to 600°C using a home-made heating device (Zema *et al.*, 2022). Seven data collections were performed at temperatures of 25, 100, 200, 300, 400, 500 and 600°C; each data collection lasted ~11 hours. Before starting a new data collection, the crystal was equilibrated for ~30 min. Data reduction was done using the software *SAINT* (Bruker, 2007); empirical absorption corrections were applied by means of *SADABS* (Bruker, 2009); structure refinements were performed with the program *CRYSTALS* (Betteridge *et al.*, 2003) in the triclinic space group $P\bar{1}$ using reflections with $I > 3\sigma(I)$ and starting from the atomic coordinates of fedorite (Gav-43 sample) reported in Kaneva *et al.* (2020a). Overall scale factor, atomic positions and atomic displacement parameters were refined. At room temperature all cation and H_2O occupancies (O20w–O24w oxygen atoms) were refined, whereas, starting from 100°C and for all data collected at higher temperatures the cation site occupancies were kept fixed, and only the H_2O site occupancies were varied to avoid unstable refinements, unreasonable cation occupancies and/or high correlations with displacement parameters. The occupancies of the tetrahedral and octahedral sites were constrained to 1. The attempts to anisotropically refine the interlayer Na cations and the oxygen of the H_2O resulted in physically unreasonable refinement parameters. Therefore, in the final refinement they were modelled isotropically. The analysis of the difference-Fourier maps showed the presence of residual electron density peaks less than 1 $e^-/Å^3$ which may be ascribed to the positional disorder of Na atoms. The modelling of this disorder, however, did not lead to a significant improvement of the refinement and was not included in the final structure model. The effective coordination numbers (ECoN) of the cations were calculated using the *ECoN21* software (Ilinca, 2022) considering the bond lengths that give a contribution >0.05 vu to the bond-valence sum (BVS) of the central cation (Brown, 2006).

The crystallographic information files have been deposited with the Principal Editor of *Mineralogical Magazine* and are available as Supplementary material (see below) together with details on structure analysis (Tables S2 to S4).

Fourier-transform infrared spectroscopy

The infrared absorption spectra of fedorite were measured using an FT-801 spectrometer (Simex, Novosibirsk, Russia). Powdered samples were mixed with anhydrous KBr, pelletised and analysed at a resolution of 1 cm^{-1}. A total of 32 scans were collected in the wavenumber range 500 to 4000 cm^{-1}. The IR spectrum of an analogous pellet of pure KBr was used as a reference.

Infrared spectra for variable temperatures, aimed at the study of fedorite dehydration were carried out *ex situ*, in the temperature range 25–700°C, in steps of 50°C following the procedure described in Kaneva *et al.* (2020a) and Sapozhnikov *et al.* (2021), summarised briefly here. Fedorite and KBr were ground in a crucible, held at a given temperature for 5 min in a muffle furnace, and then quenched to room temperature. Afterwards, two pressed pellets were prepared: one consisting of a mixture of fedorite and KBr and another one of the pure KBr. Next, powders of both samples were heated to the next temperature in the interval 25–700°C, and the procedure was repeated. All pressed pellets were prepared and measured under the same conditions of low relative humidity (<20%). This preparation means that water adsorption in heated samples can be ignored.

Results and discussion

Chemical composition

The average chemical composition of the fedorite (wt.%) from the Gav-33 rock sample, determined over ten spots, is: SiO_2 (65.74), Al_2O_3 (0.07), CaO (16.74), SrO (0.83), MnO (0.11), MgO (0.02), FeO (0.03), BaO (0.01), Na_2O (8.58), K_2O (2.28), F (2.46), Cl (0.21), total 94.68 wt.%. This composition is similar to that provided for fedorite from Gav-43 sample by Kaneva *et al.* (2020a) with the only exception for Na_2O 6.2(7) and K_2O 5.8(5) wt.%.

The crystal chemical formula of the sample studied, calculated on the basis of 16(Si+Al) and assuming the H_2O content derived by the structure refinement (see below) is reported in Table 1, where it is compared with those reported from previous investigations on fedorite.

It can be noted that Kukharenko *et al.* (1965) report only K^+ as interlayer cation whereas Sokolova *et al.* (1983), Blackburn and Dennen (1997) and Kaneva *et al.* (2020a) found K^+ and Na^+ with $K^+ \geq Na^+$. On the contrary, fedorite in Joswig *et al.* (1988), Mitchell and Burns (2001) and in this study shows $Na^+ > K^+$.

The octahedral cations are essentially Ca^{2+} and Na^+, except for minor amounts of Al^{3+}, Mn^{2+}, Fe^{2+}, Ti^{4+} and Mg^{2+} reported by Joswig *et al.* (1988), Mitchell and Burns (2001), Kaneva *et al.* (2020a) and in this work.

The fedorite of Kukharenko *et al.* (1965) and Blackburn and Dennen (1997) has no fluorine content, whereas other authors report (OH^-, F^- and Cl^-) substitutions (Sokolova *et al.*, 1983; Joswig *et al.*, 1988; Kaneva *et al.*, 2020c). The fedorite of the present work shows only (F^- and Cl^-) substitution and is similar to the samples in Mitchell and Burns (2001). OH^- groups substituting oxygen atoms are present in the formula of the crystal studied (0.07 groups per formula unit, gpfu) and in Kaneva *et al.* (2020a), from 0.30 to 0.46 gpfu, possibly indicating substitutions of bridging tetrahedral–octahedral oxygen atoms (O1–O6). More specifically, Kaneva *et al.* (2020a) provided direct evidence of the occurrence of OH^- groups from FTIR analysis. In our case, the single crystal shows almost negligible OH^- content whereas the FTIR spectrum collected from the powdered sample reveals vibrations matching OH-stretching (see below) indicating some heterogeneity of OH^- concentrations in fedorite crystals.

Fedorite is also affected by different degrees of hydration. The H_2O content derived from structure refinement was found to be 0.6 gpfu to 2.5 gpfu in Kaneva *et al.* (2020a), 3.47 and 3.69 gpfu in Mitchell and Burns (2001) and 2.8 gpfu in the present work, but higher values are also reported in Blackburn and Dennen (1997). The water content in fedorite from the Murun massif is consistent with the different temperature in the crystallisation environment of the relevant host rock as discussed in Kaneva *et al.* (2020a), see the *Geological background and sample description* above.

Thermal data

The TG/DTA/DTG experiments in air and He provided similar results (compare Fig. 1 and Fig. S3). The DTA curve shows an exothermic peak at ~950°C which may be associated with the breakdown of fedorite. The thermogravimetric analysis, instead,

https://doi.org/10.1180/mgm.2023.31 Published online by Cambridge University Press

Table 1. Crystal chemical formulae of the studied and literature fedorite.

Reference	Sample	Crystal chemical formula
Kukharenko *et al.* (1965)		$K_{0.27}(Ca_{1.02}Na_{0.93})_{\Sigma1.95}(Al_{0.20}Si_{3.80})_{\Sigma4.00}O_{9.05}(OH)_{0.95}\cdot1.5H_2O$
Sokolova *et al.* (1983)		$(K_{1.65}Na_{0.83})_{\Sigma2.48}(Ca_{4.52}Na_{2.48})_{\Sigma7.00}Si_{16}O_{38}(OH,F)_2\cdot H_2O$
Joswig *et al.* (1988)		$(K_{0.82}Na_{1.95})_{\Sigma2.77}(Ca_{4.35}Na_{2.34}Al_{0.31})_{\Sigma7.00}(Si_{15.35}Al_{0.65})O_{38}(OH,F)_2\cdot H_2O$
Blackburn and Dennen (1997)		$KNa_4Ca_4(Si,Al)_{16}O_{36}(OH)_4\cdot6H_2O$
Mitchell and Burns (2001)	Turiy	$(Na_{1.27}K_{0.92}Ba_{0.03})_{\Sigma2.22}(Ca_{4.06}Na_{2.85}Mn_{0.07}Fe_{0.02}Ti_{0.004}Mg_{0.004})_{\Sigma7.0}(Si_{16.01}Al_{0.09})_{\Sigma16.10}O_{38}(F,Cl)_{2.27}$
	Murun	$(Na_{1.68}K_{0.48})_{\Sigma2.16}(Ca_{4.41}Na_{2.54}Mn_{0.07}Fe_{0.04}Ti_{0.002})_{\Sigma7.0}(Si_{15.96}Al_{0.03})_{15.98}O_{38}(F,Cl)_{2.47}$
Kaneva *et al.* (2020a)	Gav-43	$(K_{1.78}Na_{0.23}Sr_{0.09}Ba_{0.01})_{\Sigma2.11}(Ca_{4.31}Na_{2.65}Mn_{0.02}Fe_{0.01}Mg_{0.01})_{\Sigma7.0}(Si_{15.98}Al_{0.02})_{\Sigma16.0}(O_{37.54}OH_{0.46})_{\Sigma38.0}\ (F_{1.79}Cl_{0.10}OH_{0.11})_{\Sigma2}\cdot2.5H_2O$
	Yak-5	$(K_{2.25}Na_{0.10})_{\Sigma2.35}(Ca_{4.29}Na_{2.63}Mn_{0.07}Fe_{0.01})_{\Sigma7.0}(Si_{15.98}Al_{0.02})_{\Sigma16.0}(O_{37.70}OH_{0.30})_{\Sigma38.0}(F_{1.60}Cl_{0.03}OH_{0.37})_{\Sigma2.0}\cdot0.8H_2O$
	Irk-53	$(K_{2.08}Na_{0.22}Ba_{0.03})_{\Sigma2.33}(Ca_{4.33}Na_{2.50}Mn_{0.07}Fe_{0.01})_{\Sigma7.0}(Si_{15.98}Al_{0.02})_{\Sigma16.0}(O_{37.66}OH_{0.34})_{\Sigma38.0}(F_{1.53}Cl_{0.02}OH_{0.45})_{\Sigma2.0}\cdot0.6H_2O$
This study	Gav-33	$(Na_{1.56}K_{0.72}Sr_{0.12})_{\Sigma2.40}(Ca_{4.42}Na_{2.54}Mn_{0.02}Fe_{0.01}Mg_{0.01})_{\Sigma7.00}(Si_{15.98}Al_{0.02})_{\Sigma16.00}(F_{1.92}Cl_{0.09})_{\Sigma2.01}(O_{37.93}OH_{0.07})_{\Sigma38.00}\cdot2.8H_2O$

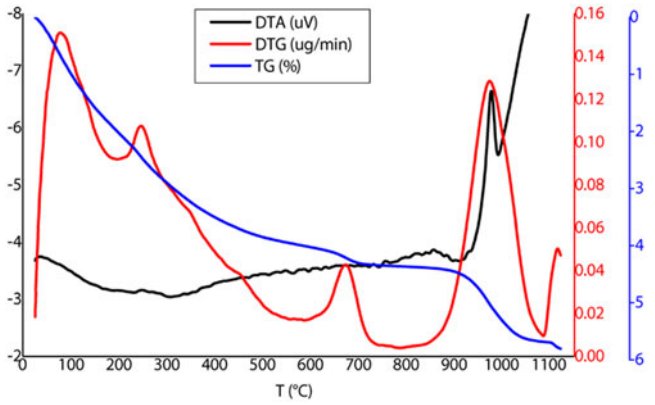

Figure 1. Differential thermal analysis (DTA, black line), thermogravimetric analysis (TG, blue line), and the TG first derivative (DTG, red line) of sample Gav-33, measured in air.

exhibits a weight mass decrease of ~4% (100–650°C temperature range) and 1.5% (1000–1050°C). The former mass decrease is compatible with a loss of 3.4 H_2O. This value is comparable with that derived from single-crystal X-ray data (2.8 H_2O gpfu, see below). The weight loss >900°C, instead, may be ascribed to the loss of fluorine as indicated by the measurement in the He atmosphere (Fig. S3).

Crystal structure at room temperature

Room temperature refinement of the Gav-33 sample of fedorite was carried out in space group $P\bar{1}$ and converged to $R_1 = 2.96\%$, $wR_2 = 3.61\%$ (Table 2). Unit-cell parameters and cell volume (a = 9.6458(2), b = 9.6521(2), c = 12.6206(4) Å, α = 102.458(2), β = 96.2250(10), γ = 119.9020(10)° and V = 961.69(5) Å^3; Table 2) are almost identical to those reported in literature (Mitchell and Burns, 2001; Kaneva *et al.* 2020a). Atomic coordinates, site occupancy and displacement parameters are reported in Table 3 and 4; bond distances, bond-length distortion, effective coordination numbers (ECoN) and bond-valence sums (BVS) of the central cations, are listed in Tables 5 and S4. Tables 3, 4 and 5 contain data at 25°C which are compared with those collected at 400°C, whereas data obtained at higher temperatures are reported in the supplementary materials. A general view of the crystal

Table 2. Selected crystallographic data and experimental conditions for the studied fedorite (Gav-33 sample) at room temperature and from 100 to 600°C.

	25°C	100°C	200°C	300°C	400°C	500°C	600°C
Crystal data							
Space group	$P\bar{1}$	$P\bar{1}$	$P\bar{1}$	$P\bar{1}$	$P\bar{1}$	$P\bar{1}$	$P\bar{1}$
a (Å)	9.6458(2)	9.647(6)	9.6622(2)	9.6695(3)	9.6767(3)	9.6821(2)	9.6878(2)
b (Å)	9.6521(2)	9.683(9)	9.6653(2)	9.6724(3)	9.6795(3)	9.6863(2)	9.6888(3)
c (Å)	12.6206(4)	12.583(9)	12.5579(3)	12.5669(4)	12.5673(4)	12.5643(3)	12.5606(3)
α (°)	102.458(2)	102.07(6)	102.3710(10)	102.409(2)	102.396(2)	102.4210(10)	102.4460(10)
β (°)	96.2250(10)	96.51(5)	96.2860(10)	96.225(2)	96.2620(10)	96.2680(10)	96.2790(10)
γ (°)	119.9020(10)	119.97(5)	119.9050(10)	119.8860(10)	119.8750(10)	119.8550(10)	119.8500(10)
V (Å^3)	961.69(5)	962.3(15)	960.06(4)	962.31(6)	963.94(6)	964.95(4)	965.32(4)
Data collection							
Measured reflections	50507	36537	36514	36545	36663	36917	36957
Independent reflections	13021	12074	12048	12058	12088	12119	12121
$R_{merging}$ [$R_{(int)}$] (%)	2.77	3.11	3.10	3.21	3.29	3.20	3.21
h_{min}, h_{max}	−17, 18	−17, 17	−17, 17	−17, 17	−17, 17	−17, 17	−17, 17
k_{min}, k_{max}	−18, 18	−13, 17	−13, 17	−13, 17	−13, 17	−13, 17	−13, 17
l_{min}, l_{max}	−22, 22	−21, 22	−21, 22	−21, 22	−21, 22	−21, 22	−21, 22
Refinement							
Reflections used [$I > 3\sigma(I)$]	9810	9026	8772	8443	8215	8189	7834
No. of refined parameters	362	353	348	348	333	333	333
Goof [a]	0.965	0.949	0.968	0.932	0.907	0.982	0.947
R_1 [b] [on F] (%)	2.96	3.15	3.27	3.34	3.37	3.38	3.47
wR_2 [c] [on F^2] (%)	3.61	3.87	3.82	4.39	4.61	4.03	4.28
$\Delta\rho_{min}/\Delta\rho_{max}$ (e^-/Å^3)	−0.80/0.88	−0.77/0.96	−0.77/0.92	−0.79/0.85	−0.53/0.67	−0.58/0.65	−0.57/0.62

[a]Goodness of fit = $[\Sigma[w(F_o^2-F_c^2)^2]/(N-p)]^{½}$, where N and p are the number of reflections and parameters, respectively.
[b]$R_1 = \Sigma[|F_o| - |F_c|]/\Sigma|F_o|$.
[c]$_wR_2 = [\Sigma[w(F_o^2-F_c^2)^2]/\Sigma[w(F_o^2)^2]]^{½}$, w = 1.0/[A[0]*T[0]'(X)+A[1]*T[1]'(X) … +A[NP−1]*T[NP−1]'(X)] (Chebyshev optimised weights). The optimised parameters for each refinement are reported in the deposited Crystallographic Information Files.

https://doi.org/10.1180/mgm.2023.31 Published online by Cambridge University Press

Table 3. Crystallographic coordinates, occupancies, equivalent isotropic (Å^2) and anisotropic displacement parameters of the fedorite studied at 25°C.

Site	Atom	*x/a*	*y/b*	*z/c*	Occupancy	$U_{iso/equivalent}$	U^{11}	U^{22}	U^{33}	U^{12}	U^{13}	U^{23}
*Na*1	Na	0	0	½	0.724(5)	0.01350(12)	0.0122(3)	0.0126(3)	0.0161(3)	0.0067(2)	0.0034(2)	0.0049(2)
*Ca*1	Ca	0	0	½	0.276(5)	0.01350(12)	0.0122(3)	0.0126(3)	0.0161(3)	0.0067(2)	0.0034(2)	0.0049(2)
*Na*2	Na	0.42209(4)	0.28437(4)	0.50926(3)	0.430(4)	0.01110(6)	0.01058(13)	0.00972(13)	0.01305(15)	0.00553(10)	0.00308(10)	0.00318(10)
*Ca*2	Ca	0.42209(4)	0.28437(4)	0.50926(3)	0.570(4)	0.01110(6)	0.01058(13)	0.00972(13)	0.01305(15)	0.00553(10)	0.00308(10)	0.00318(10)
*Na*3	Na	0.71116(3)	0.14776(3)	0.50058(2)	0.159(4)	0.01030(5)	0.01013(11)	0.00901(11)	0.01219(12)	0.00505(8)	0.00335(8)	0.00406(8)
*Ca*3	Ca	0.71116(3)	0.14776(3)	0.50058(2)	0.841(4)	0.01030(5)	0.01013(11)	0.00901(11)	0.01219(12)	0.00505(8)	0.00335(8)	0.00406(8)
*Na*4	Na	0.14893(4)	0.43328(4)	0.51542(3)	0.248(4)	0.01060(5)	0.00961(11)	0.00963(12)	0.01257(13)	0.00509(9)	0.00308(8)	0.00382(9)
*Ca*4	Ca	0.14893(4)	0.43328(4)	0.51542(3)	0.752(4)	0.01060(5)	0.00961(11)	0.00963(12)	0.01257(13)	0.00509(9)	0.00308(8)	0.00382(9)
*Si*1	Si	0.28417(4)	0.60265(4)	0.86964(3)	1	0.00800(5)	0.00803(12)	0.00716(12)	0.00887(13)	0.00405(10)	0.00237(10)	0.00262(10)
*Si*2	Si	0.13889(4)	0.74282(4)	0.72956(3)	1	0.00830(5)	0.00761(12)	0.00702(12)	0.01073(13)	0.00372(10)	0.00290(10)	0.00383(10)
*Si*3	Si	0.76818(4)	0.49706(4)	0.72701(3)	1	0.00860(5)	0.00737(12)	0.00781(12)	0.01224(14)	0.00436(10)	0.00385(10)	0.00453(10)
*Si*4	Si	0.26388(4)	0.10937(4)	0.72921(3)	1	0.00900(5)	0.00770(12)	0.00746(12)	0.01249(14)	0.00444(10)	0.00206(10)	0.00345(10)
*Si*5	Si	0.02033(4)	0.24151(4)	0.73239(3)	1	0.00860(5)	0.00692(11)	0.00722(12)	0.01158(14)	0.00374(10)	0.00222(10)	0.00292(10)
*Si*6	Si	0.39013(4)	0.73683(4)	0.13712(3)	1	0.00770(5)	0.00775(11)	0.00715(11)	0.00827(13)	0.00391(10)	0.00202(9)	0.00254(10)
*Si*7	Si	0.65198(4)	−0.00440(4)	0.72925(3)	1	0.00850(5)	0.00827(12)	0.00626(11)	0.01109(13)	0.00376(10)	0.00366(10)	0.00284(10)
*Si*8	Si	0.52827(4)	0.62709(4)	0.73249(3)	1	0.00890(5)	0.00851(12)	0.00746(12)	0.01178(14)	0.00491(10)	0.00313(10)	0.00294(10)
O1	O	0.70317(15)	0.38674(15)	0.59868(10)	1	0.01790(17)	0.0198(4)	0.0179(4)	0.0138(4)	0.0112(4)	−0.0001(3)	0.0002(3)
O2	O	0.12939(15)	0.66914(14)	0.60160(9)	1	0.01720(19)	0.0249(5)	0.0160(4)	0.0131(4)	0.0118(4)	0.0085(4)	0.0048(3)
O3	O	0.27792(16)	0.08305(15)	0.60354(10)	1	0.0197(2)	0.0259(5)	0.0194(5)	0.0133(4)	0.0113(4)	0.0064(4)	0.0057(4)
O4	O	0.42200(17)	0.52858(19)	0.60659(11)	1	0.0262(2)	0.0236(5)	0.0318(6)	0.0174(5)	0.0184(5)	−0.0054(4)	−0.0067(4)
O5	O	0.01497(16)	0.75395(17)	0.39190(10)	1	0.0219(2)	0.0192(5)	0.0270(6)	0.0148(5)	0.0077(4)	0.0037(4)	0.0105(4)
O6	O	0.57088(14)	0.95553(14)	0.60135(9)	1	0.01670(17)	0.0172(4)	0.0184(4)	0.0108(4)	0.0076(4)	0.0023(3)	0.0039(3)
O7	O	0.85278(12)	0.12073(13)	0.76602(10)	1	0.01490(18)	0.0090(3)	0.0125(4)	0.0198(5)	0.0031(3)	0.0052(3)	0.0051(3)
O8	O	0.67603(13)	0.59568(14)	0.76262(10)	1	0.01530(18)	0.0157(4)	0.0182(4)	0.0211(5)	0.0137(4)	0.0082(3)	0.0090(4)
O9	O	0.19349(13)	0.93832(12)	0.76497(9)	1	0.01440(16)	0.0153(4)	0.0070(3)	0.0197(4)	0.0053(3)	0.0029(3)	0.0051(3)
O10	O	0.62515(14)	0.82964(13)	0.75925(11)	1	0.01750(19)	0.0197(4)	0.0098(4)	0.0281(5)	0.0090(3)	0.0108(4)	0.0098(4)
O11	O	0.43853(12)	0.25116(12)	0.82224(10)	1	0.01450(17)	0.0089(3)	0.0095(3)	0.0216(5)	0.0046(3)	−0.0003(3)	0.0015(3)
O12	O	0.58256(13)	0.07927(12)	0.81732(9)	1	0.01390(16)	0.0153(4)	0.0094(3)	0.0199(4)	0.0075(3)	0.0098(3)	0.0047(3)
O13	O	0.42528(15)	0.58079(16)	0.82663(11)	1	0.0192(2)	0.0196(4)	0.0239(5)	0.0303(6)	0.0168(4)	0.0180(4)	0.0184(4)
O14	O	0.26657(13)	0.73381(14)	0.81854(10)	1	0.01660(19)	0.0126(4)	0.0138(4)	0.0244(5)	0.0069(3)	0.0006(3)	0.0103(4)
O15	O	0.03917(12)	0.35120(13)	0.24091(10)	1	0.01580(18)	0.0084(3)	0.0140(4)	0.0230(5)	0.0031(3)	0.0063(3)	0.0084(3)
O16	O	0.11104(13)	0.42380(12)	0.82871(10)	1	0.01670(19)	0.0117(4)	0.0082(3)	0.0230(5)	0.0023(3)	0.0049(3)	−0.0002(3)
O17	O	0.13233(13)	0.16297(14)	0.75221(12)	1	0.0196(2)	0.0124(4)	0.0155(4)	0.0346(6)	0.0107(3)	0.0048(4)	0.0066(4)
O18	O	0.75232(13)	0.39197(14)	0.81503(10)	1	0.01600(19)	0.0126(4)	0.0170(4)	0.0252(5)	0.0084(3)	0.0087(3)	0.0155(4)
O19	O	0.33330(19)	0.67261(19)	0.00315(10)	1	0.0261(3)	0.0325(6)	0.0307(6)	0.0087(4)	0.0156(5)	0.0001(4)	0.0005(4)
F	F	0.15989(13)	0.20586(14)	0.41823(9)	1	0.02140(16)	0.0206(4)	0.0220(4)	0.0206(4)	0.0115(4)	0.0043(3)	0.0052(4)
*Na*5	Na	0.0829(2)	0.1043(3)	0.2138(3)	0.569(8)	0.0232(4)	0.0152(6)	0.0173(6)	0.0410(12)	0.0094(5)	0.0109(7)	0.0125(8)
K	K	0.0650(6)	0.0830(6)	0.1661(7)	0.216(5)	0.0483(6)	0.0413(17)	0.0436(18)	0.067(3)	0.0243(14)	0.019(2)	0.023(2)
*Na*6	Na	0.6612(8)	−0.0212(6)	−0.0003(3)	0.267(5)	0.0610(14)	0.113(4)	0.042(2)	0.0148(16)	0.036(3)	0.003(2)	0.0045(14)
*Na*7	Na	0.6930(8)	0.6609(8)	0.0016(3)	0.295(5)	0.0716(16)	0.103(4)	0.115(4)	0.0215(18)	0.082(4)	0.007(2)	0.010(2)
*Na*8	Na	0.9835(5)	0.3296(7)	0.0034(3)	0.258(5)	0.0460(9)	0.0293(18)	0.078(3)	0.0048(12)	0.0152(19)	0.0019(11)	0.0021(14)
O20w	O	0	0	0	0.555(9)	0.119(4)	-	-	-	-	-	-
O21w	O	0.153(3)	−0.022(3)	0.002(2)	0.318(8)	0.224(8)	-	-	-	-	-	-
O22w	O	−0.020(4)	0.281(5)	0.003(3)	0.282(9)	0.277(9)	-	-	-	-	-	-
O23w	O	0.033(3)	0.155(3)	0.0007(18)	0.244(8)	0.138(7)	-	-	-	-	-	-
O24w	O	0.165(3)	0.158(3)	−0.0019(17)	0.332(8)	0.175(6)	-	-	-	-	-	-

Table 4. Crystallographic coordinates, occupancies, equivalent isotropic (Å^2) and anisotropic displacement parameters of the studied fedorite at 400°C.

Site	Atom	*x/a*	*y/b*	*z/c*	Occupancy	$U_{iso/equivalent}$	U^{11}	U^{22}	U^{33}	U^{12}	U^{13}	U^{23}
*Na*1	Na	0	0	½	0.7236	0.0299(18)	0.0282(4)	0.0292(4)	0.0320(5)	0.0157(4)	0.0064(4)	0.0090(4)
*Ca*1	Ca	0	0	½	0.2765	0.0299(18)	0.0282(4)	0.0292(4)	0.0320(5)	0.0157(4)	0.0064(4)	0.0090(4)
*Na*2	Na	0.42408(6)	0.28579(6)	0.51114(4)	0.4298	0.02130(8)	0.02024(18)	0.01968(18)	0.0242(2)	0.01119(15)	0.00558(15)	0.00607(15)
*Ca*2	Ca	0.42408(6)	0.28579(6)	0.51114(4)	0.5702	0.02130(8)	0.02024(18)	0.01968(18)	0.0242(2)	0.01119(15)	0.00558(15)	0.00607(15)
*Na*3	Na	0.71218(5)	0.14800(5)	0.50102(3)	0.1593	0.01820(6)	0.01806(13)	0.01656(13)	0.02102(15)	0.00939(11)	0.00609(11)	0.00700(11)
*Ca*3	Ca	0.71218(5)	0.14800(5)	0.50102(3)	0.8408	0.01820(7)	0.01806(13)	0.01656(13)	0.02102(15)	0.00939(11)	0.00609(11)	0.00700(11)
*Na*4	Na	0.15003(5)	0.43539(5)	0.51796(4)	0.2482	0.01970(7)	0.01827(14)	0.01878(15)	0.02328(17)	0.01030(12)	0.00589(13)	0.00745(13)
*Ca*4	Ca	0.15003(5)	0.43539(5)	0.51796(4)	0.7518	0.01970(7)	0.01827(14)	0.01878(15)	0.02328(17)	0.01030(12)	0.00589(13)	0.00745(13)
*Si*1	Si	0.28402(5)	0.60121(5)	0.86980(4)	1	0.01340(7)	0.01376(16)	0.01333(16)	0.01259(17)	0.00724(13)	0.00302(13)	0.00364(13)
*Si*2	Si	0.13769(5)	0.74207(5)	0.73069(4)	1	0.01370(7)	0.01254(15)	0.01238(16)	0.01728(18)	0.00658(13)	0.00429(13)	0.00662(13)
*Si*3	Si	0.76850(5)	0.49785(5)	0.72825(4)	1	0.01400(7)	0.01252(15)	0.01347(16)	0.01834(18)	0.00753(13)	0.00591(14)	0.00698(14)
*Si*4	Si	0.26393(5)	0.10800(5)	0.73064(4)	1	0.01460(7)	0.01288(16)	0.01260(16)	0.01920(19)	0.00749(13)	0.00315(14)	0.00522(14)
*Si*5	Si	0.02178(5)	0.24097(5)	0.73435(4)	1	0.01440(7)	0.01127(15)	0.01232(16)	0.01894(19)	0.00612(13)	0.00339(13)	0.00469(14)
*Si*6	Si	0.39031(5)	0.73751(5)	0.13699(4)	1	0.01300(6)	0.01364(15)	0.01282(15)	0.01220(16)	0.00706(13)	0.00288(13)	0.00348(12)
*Si*7	Si	0.65354(5)	−0.00374(5)	0.73079(4)	1	0.01400(7)	0.01334(16)	0.01071(15)	0.01829(18)	0.00641(13)	0.00538(14)	0.00434(13)
*Si*8	Si	0.52942(5)	0.62851(5)	0.73405(4)	1	0.01450(7)	0.01423(16)	0.01257(16)	0.01908(19)	0.00840(14)	0.00579(14)	0.00540(14)
O1	O	0.7047(2)	0.3877(2)	0.59924(13)	1	0.0287(3)	0.0317(7)	0.0285(7)	0.0224(6)	0.0170(6)	0.0027(5)	0.0016(5)
O2	O	0.1279(2)	0.6700(2)	0.60191(13)	1	0.0271(3)	0.0367(8)	0.0261(6)	0.0201(6)	0.0174(6)	0.0114(5)	0.0065(5)
O3	O	0.2773(2)	0.0814(2)	0.60415(14)	1	0.0310(3)	0.0410(9)	0.0329(8)	0.0227(6)	0.0212(7)	0.0111(6)	0.0103(6)
O4	O	0.4231(2)	0.5302(2)	0.60791(15)	1	0.0371(3)	0.0332(8)	0.0422(9)	0.0259(7)	0.0223(7)	−0.0059(6)	−0.0062(7)
O5	O	0.0136(2)	0.7530(2)	0.38976(15)	1	0.0337(3)	0.0302(7)	0.0423(9)	0.0249(7)	0.0145(7)	0.0063(6)	0.0171(7)
O6	O	0.5718(2)	0.9558(2)	0.60220(13)	1	0.0274(3)	0.0283(7)	0.0300(7)	0.0192(6)	0.0132(6)	0.0037(5)	0.0066(5)
O7	O	0.85405(16)	0.11943(18)	0.76681(14)	1	0.0260(3)	0.0136(5)	0.0222(6)	0.0363(8)	0.0047(4)	0.0090(5)	0.0100(5)
O8	O	0.67638(19)	0.5963(2)	0.76245(14)	1	0.0266(3)	0.0254(6)	0.0312(7)	0.0370(8)	0.0230(6)	0.0126(6)	0.0130(6)
O9	O	0.19259(19)	0.93683(17)	0.76617(14)	1	0.0249(3)	0.0281(6)	0.0139(5)	0.0334(7)	0.0109(5)	0.0076(5)	0.0101(5)
O10	O	0.6269(2)	0.83055(17)	0.76049(16)	1	0.0290(3)	0.0311(7)	0.0150(5)	0.0463(9)	0.0135(5)	0.0140(6)	0.0143(6)
O11	O	0.43783(16)	0.24798(18)	0.82296(14)	1	0.0264(3)	0.0146(5)	0.0188(5)	0.0376(8)	0.0083(4)	−0.0032(5)	0.0007(5)
O12	O	0.58565(19)	0.08081(17)	0.81836(14)	1	0.0251(3)	0.0288(6)	0.0175(5)	0.0354(7)	0.0148(5)	0.0180(6)	0.0083(5)
O13	O	0.4268(2)	0.5833(2)	0.82806(16)	1	0.0322(3)	0.0345(8)	0.0418(9)	0.0475(9)	0.0294(7)	0.0304(7)	0.0295(8)
O14	O	0.26302(19)	0.7291(2)	0.81791(16)	1	0.0310(3)	0.0240(6)	0.0273(7)	0.0439(9)	0.0137(5)	0.0003(6)	0.0196(7)
O15	O	0.04011(17)	0.35045(19)	0.24006(15)	1	0.0277(3)	0.0146(5)	0.0242(6)	0.0401(8)	0.0056(5)	0.0113(5)	0.0128(6)
O16	O	0.11429(18)	0.42158(17)	0.83139(15)	1	0.0304(3)	0.0213(6)	0.0144(5)	0.0401(9)	0.0032(4)	0.0074(6)	−0.0022(5)
O17	O	0.13129(19)	0.1599(2)	0.75239(17)	1	0.0315(3)	0.0211(6)	0.0289(7)	0.0540(10)	0.0196(6)	0.0100(6)	0.0137(7)
O18	O	0.75081(18)	0.3920(2)	0.81522(15)	1	0.0276(3)	0.0229(6)	0.0306(7)	0.0403(8)	0.0147(5)	0.0143(6)	0.0265(6)
O19	O	0.3335(2)	0.6732(2)	0.00345(13)	1	0.0368(3)	0.0448(10)	0.0436(10)	0.0127(5)	0.0209(8)	0.0023(6)	0.0019(6)
F	F	0.1623(2)	0.2093(2)	0.41958(13)	1	0.0365(3)	0.0364(7)	0.0383(8)	0.0326(7)	0.0207(6)	0.0058(6)	0.0069(6)
*Na*5	Na	0.0877(5)	0.1102(5)	0.2256(3)	0.5686	0.0287(5)	0.0236(12)	0.0246(12)	0.0407(11)	0.0146(10)	0.0100(9)	0.0100(9)
K	K	0.0840(15)	0.1084(15)	0.2140(11)	0.2162	0.089(2)	0.056(4)	0.068(4)	0.165(7)	0.036(3)	0.044(4)	0.064(4)
*Na*6	Na	0.638(3)	−0.0210(18)	0.0023(9)	0.2673	0.226(4)	0.403(9)	0.112(7)	0.055(5)	0.003(8)	0.022(7)	0.017(5)
*Na*7	Na	0.663(4)	0.639(3)	0.0006(15)	0.2946	0.359(4)	0.726(9)	0.429(8)	0.134(8)	0.497(7)	0.010(8)	0.035(7)
*Na*8	Na	0.9825(15)	0.363(3)	0.0044(8)	0.2575	0.266(3)	0.078(5)	0.538(9)	0.042(4)	0.106(8)	0.015(4)	−0.009(8)
O20w	O	0	0	0	0.419(9)	0.220(8)	-	-	-	-	-	-

structure of fedorite is given in Fig. 2. In particular, Fig. 2b shows the regular hexagonal ring of downward-pointing tetrahedra and the distorted hexagonal ring composed of four downward-pointing tetrahedra and two upward-pointing tetrahedra extending in the *ab* plane, whereas Fig. 2a shows that the connection between single tetrahedral sheets occurs via *Si*1 and *Si*6 tetrahedra sharing the apical O19 oxygen. The *Si*1 and *Si*6 tetrahedra show slightly short mean tetrahedral distances due to the low values of the *Si*1–O19 and *Si*6–O19 individual distances (Fig. 2a; Table 5). The four symmetrically independent octahedra (*M*1 to *M*4) of fedorite exhibit mixed Na,Ca occupancy. In detail, X-ray site-scattering refinement indicates a preferential partitioning of Na for the octahedral *M*1 site, an almost equal distribution of Na and Ca at *M*2, and the prevalence of Ca at *M*3 and *M*4 sites (Tables 3, 4). Similar octahedral site occupancies were reported for other fedorite from Murun by Kaneva *et al.* (2020a). The $M1O_4^{2-}F_2^-$ octahedron, exhibits the longest average bond distance and the highest bond-length distortion (BLD parameter) whereas the $M3O_6^{2-}$ octahedron is more regular (Table 5).

The interstitial complex of fedorite consists of Na and K atoms at *Na*5, *K*, *Na*6, *Na*7 and *Na*8 sites. In detail, the *Na*5 and *K* sites site are separated by 0.568(6) Å and are occupied by 57% Na and 22% K, respectively. The coordination polyhedron of the cation at the *Na*5 site contains eight ligands (six oxygen atoms of the tetrahedral ring, one H_2O at O20w position and one F atom), see Tables 5, S4. The coordination polyhedron around the atom at the *K* site consists of six oxygens of the tetrahedral ring and one F atom (Table S4). Finally, the *Na*6 to *Na*8 sites are characterised by low Na occupancy (26–30%, Tables 3, 4) and an ill-defined coordination environment (Table S4).

Occupancy refinement of the five H_2O positions (O20w to O24w) of our Gav-33 sample showed that the O20w site is the most populated, with occupancy of 56% versus 53% refined by Kaneva *et al.* (2020a) for sample Gav-43. The O21w to O24w sites have occupancy in the range 24–33% in Gav-33 versus 20–32% in Gav 43. The refinement also shows short *K*–O20w, *Na*6–O21w, *Na*7–O24w, *Na*8–O22w and *Na*8–O23w distances (1.980(8), 1.63(3), 1.60(2), 0.45(5) and 1.96(3) Å, respectively) indicating atom disorder and the occurrence of a range of configurations, from partially occupied sites to mutually exclusive positions. Short distances between H_2O (1.36(2)–1.59(3) Å) point to a statistical distribution of the molecules.

https://doi.org/10.1180/mgm.2023.31 Published online by Cambridge University Press

Table 5. Selected bond distances (Å), effective coordination number (ECoN), bond-valence sums (BVS, vu) and bond-length distortion (BLD parameter, %) derived from the structure refinement of the studied fedorite at 25 and 400°C.

	25°C	400°C		25°C	400°C		25°C	400°C
*Si*1–O13	1.6090(11)	1.6038(14)	*Si*4–O3	1.5828(12)	1.5849(17)	*Si*7–O6	1.5882(11)	1.5911(16)
*Si*1–O14	1.6095(11)	1.6026(15)	*Si*4–O9	1.6311(10)	1.6329(14)	*Si*7–O7	1.6298(10)	1.6319(14)
*Si*1–O16	1.6092(10)	1.6049(14)	*Si*4–O11	1.6336(10)	1.6253(14)	*Si*7–O10	1.6266(11)	1.6262(14)
*Si*1–O19	1.5926(12)	1.5893(16)	*Si*4–O17	1.6222(11)	1.6229(14)	*Si*7–O12	1.6277(10)	1.6184(14)
<*Si*1–O>	1.605(2)	1.600(3)	<*Si*4–O>	1.618(2)	1.617(3)	<*Si*7–O>	1.618(2)	1.617(3)
ECoN	4.00	4.00	ECoN	3.98	3.98	ECoN	3.99	3.99
BVS	4.21	4.27	BVS	4.08	4.09	BVS	4.07	4.08
BLD_{Si1}	0.35	0.33	BLD_{Si4}	1.02	0.93	BLD_{Si7}	0.87	0.78
*Si*2–O2	1.5905(11)	1.5909(15)	*Si*5–O5	1.5834(12)	1.5797(17)	*Si*8–O4	1.5820(13)	1.5804(17)
*Si*2–O9	1.6224(10)	1.6200(14)	*Si*5–O7	1.6233(10)	1.6227(14)	*Si*8–O8	1.6220(10)	1.6207(14)
*Si*2–O14	1.6231(11)	1.6149(15)	*Si*5–O16	1.6281(11)	1.6224(15)	*Si*8–O10	1.6231(11)	1.6247(14)
*Si*2–O15	1.6257(10)	1.6253(14)	*Si*5–O17	1.6261(11)	1.6259(14)	*Si*8–O13	1.6250(11)	1.6179(15)
<*Si*2–O>	1.615(2)	1.613(2)	<*Si*5–O>	1.615(2)	1.613(3)	<*Si*8–O>	1.613(2)	1.611(3)
ECoN	3.99	3.99	ECoN	3.98	3.98	ECoN	3.98	3.98
BVS	4.10	4.13	BVS	4.10	4.13	BVS	4.10	4.15
BLD_{Si2}	0.71	0.65	BLD_{Si5}	0.93	0.95	BLD_{Si8}	0.90	0.90
*Si*3–O1	1.5875(12)	1.5907(16)	*Si*6–O11	1.6147(10)	1.6102(14)	*Na*5–O7	2.591(2)	2.568(5)
*Si*3–O8	1.6260(10)	1.6249(14)	*Si*6–O12	1.6160(10)	1.6130(14)	*Na*5–O8	2.578(2)	2.567(5)
*Si*3–O15	1.6216(10)	1.6197(14)	*Si*6–O18	1.6121(10)	1.6104(14)	*Na*5–O9	2.542(2)	2.535(4)
*Si*3–O18	1.6294(11)	1.6191(14)	*Si*6–O19	1.5973(12)	1.5860(16)	*Na*5–O10	2.522(2)	2.503(4)
<*Si*3–O>	1.616(2)	1.614(3)	<*Si*6–O>	1.610(2)	1.605(3)	*Na*5–O15	2.580(2)	2.560(4)
ECoN	3.99	3.99	ECoN	4.00	3.99	*Na*5–O17	2.545(2)	2.514(5)
BVS	4.09	4.12	BVS	4.16	4.22	*Na*5–O20w	2.548(3)	2.678(3)
BLD_{Si3}	0.82	0.67	BLD_{Si6}	0.38	0.54	*Na*5–O21w	2.98(3)	–
						*Na*5–O21w’	3.02(3)	–
*M*1 position:	(*Na*1*Ca*1)		*M*2 position:	(*Na*2*Ca*2)		*Na*5–O23w	2.87(2)	–
*M*1–O3 (x2)	2.4865(13)	2.4937(19)	*M*2–O1	2.4052(12)	2.4038(17)	*Na*5–O23w’	2.91(2)	–
*M*1–O5 (x2)	2.5513(15)	2.566(2)	*M*2–O3	2.4058(12)	2.4191(18)	*Na*5–O24w	2.99(2)	–
*M*1–F (x2)	2.3593(11)	2.3769(17)	*M*2–O4	2.4121(13)	2.4216(19)	*Na*5–O24w’	2.99(2)	–
<*M*1–O, F>	2.466(3)	2.479(5)	*M*2–O4’	2.5628(17)	2.569(2)	*Na*5–F	2.436(4)	2.304(4)
ECoN	6.65	6.73	*M*2–O6	2.4694(12)	2.4850(17)			
BVS	1.03	1.00	*M*2–F	2.3182(11)	2.3278(17)	*Na*6–O7	3.794(5)	3.901(15)
BLD_{M1}	3.26	3.18	<*M*2–O, F>	2.429(3)	2.438(4)	*Na*6–O9	2.895(4)	2.902(14)
			ECoN	5.94	5.90	*Na*6–O10	2.965(4)	3.034(13)
			BVS	1.10	1.36	*Na*6–O11	3.375(5)	3.316(14)
			BLD_{M2}	3.04	3.04	*Na*6–O12	2.851(4)	2.793(15)
						*Na*6–O12’	3.405(6)	3.238(18)
*M*3 position:	(*Na*3*Ca*3)		*M*4 position:	(*Na*4*Ca*4)		*Na*6–O13	3.360(5)	3.356(14)
*M*3–O1	2.4136(11)	2.4227(16)	*M*4–O1	2.4861(13)	2.4930(18)	*Na*6–O14	2.902(4)	2.846(15)
*M*3–O2	2.4197(12)	2.4231(16)	*M*4–O2	2.4960(13)	2.5031(18)	*Na*6–O14’	3.480(6)	3.379(19)
*M*3–O3	2.3879(13)	2.3841(17)	*M*4–O2’	2.4094(11)	2.4128(16)	*Na*6–O15	3.910(5)	3.987(15)
*M*3–O5	2.4266(13)	2.4397(18)	*M*4–O4	2.3619(13)	2.3646(18)	*Na*6–O19	3.083(6)	2.965(16)
*M*3–O6	2.4040(12)	2.4077(16)	*M*4–O5	2.3659(12)	2.3684(17)	*Na*6–O19’	3.347(5)	3.258(19)
*M*3–O6’	2.4563(12)	2.4812(16)	*M*4–F	2.3308(11)	2.3367(17)	*Na*6–O20w	3.171(7)	3.41(3)
<*M*3–O>	2.418(3)	2.427(4)	<*M*2–O, F>	2.408(3)	2.413(4)	*Na*6–O22w	3.00(4)	–
ECoN	5.99	5.97	EcoN	5.92	5.91	*Na*6–O23w	3.10(3)	–
BVS	1.68	1.64	BVS	1.59	1.56	*Na*6–O23w’	3.77(3)	–
BLD_{M3}	0.86	1.22	BLD_{M4}	7.27	2.61	*Na*6–O24w	2.60(2)	–
K–O7	2.714(5)	2.607(12)	*Na*7–O8	2.914(4)	2.96(2)	*Na*8–O7	2.945(4)	3.045(12)
K–O8	2.693(5)	2.553(12)	*Na*7–O9	3.873(5)	3.951(18)	*Na*8–O8	3.826(4)	3.969(15)
K–O9	2.655(5)	2.538(12)	*Na*7–O10	3.901(5)	3.932(19)	*Na*8–O12	3.546(4)	3.539(12)
K–O10	2.658(5)	2.521(12)	*Na*7–O11	2.853(5)	2.75(2)	*Na*8–O14	3.397(4)	3.366(11)
K–O15	2.701(5)	2.543(12)	*Na*7–O11’	3.471(6)	3.34(2)	*Na*8–O15	2.930(4)	2.995(14)
K–O17	2.701(5)	2.556(12)	*Na*7–O13	2.860(5)	2.72(2)	*Na*8–O16	2.746(4)	2.662(12)
K–O20w	–	2.541(13)	*Na*7–O13’	3.392(6)	3.25(2)	*Na*8–O16’	3.375(5)	3.161(16)
K–O21w	2.53(3)	–	*Na*7–O16	3.201(5)	3.204(19)	*Na*8–O18	2.866(4)	2.782(12)
K–O21w’	2.55(3)	–	*Na*7–O17	3.018(4)	3.097(19)	*Na*8–O18’	3.434(5)	3.239(16)
K–O22w	3.39(4)	–	*Na*7–O18	3.428(5)	3.46(2)	*Na*8–O19	3.037(5)	2.886(13)
K–O22w’	3.48(4)	–	*Na*7–O19	3.087(6)	3.032(17)	*Na*8–O19’	3.349(5)	3.226(16)
K–O24w (x2)	2.53(2)	–	*Na*7–O19’	3.529(6)	3.36(3)	*Na*8–O20w	3.255(6)	3.59(2)
K–F	3.004(8)	2.440(13)	*Na*7–O20w	3.140(7)	3.39(3)	*Na*8–O21w	2.56(3)	–
			*Na*7–O21w	3.05(3)	–	*Na*8–O24w	2.95(2)	–
			*Na*7–O22w	2.92(4)	–			

BVS = $\Sigma s_{ij} = \Sigma_j \exp[(R_O - R_{ij})/B]$, where R_{ij} is the bond length between ions *i* and *j*, s_{ij} is the bond valence, R_O and *B* are the bond-valence parameters (Brown and Altermatt, 1985; Brese and O’Keeffe, 1991). For sites with mixed site occupancy, weighted bond-valence sums are given. BLD parameter error estimated by varying the refined positional parameters within one standard deviation is in the 0.1–13% range.

https://doi.org/10.1180/mgm.2023.31 Published online by Cambridge University Press

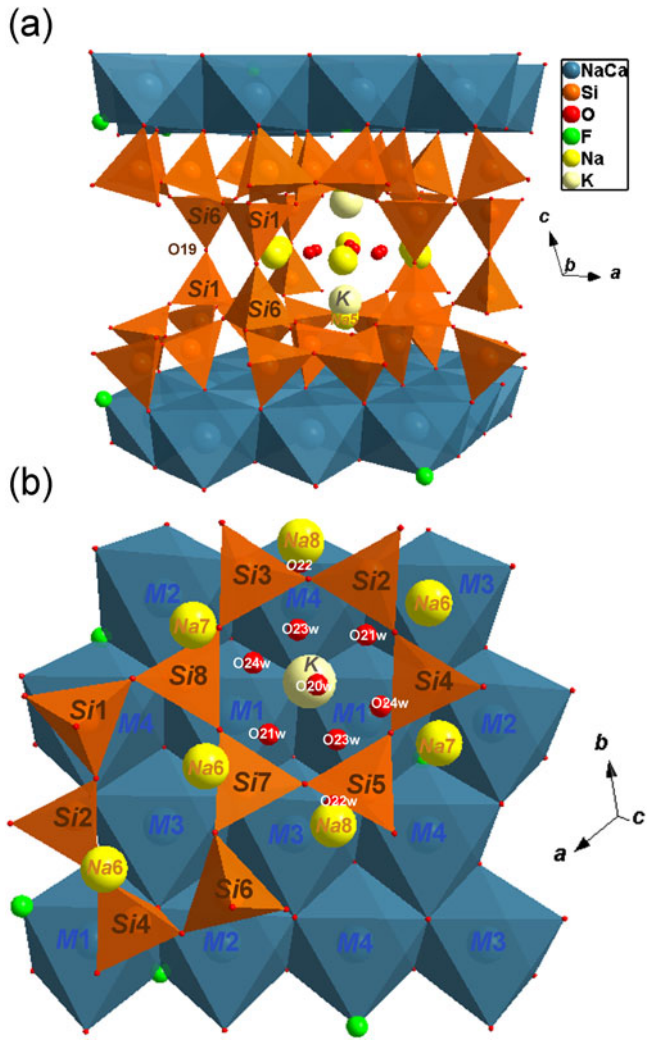

Figure 2. (a) Crystal structure of the fedorite sample, Gav-33; (b) a detail, as seen along [001], of tetrahedral (orange) and octahedral (blue) sites. Interlayer site occupied by Na^+ (dark yellow) and K^+ (light yellow) cations. Oxygen and fluorine atoms are represented in red and green, respectively.

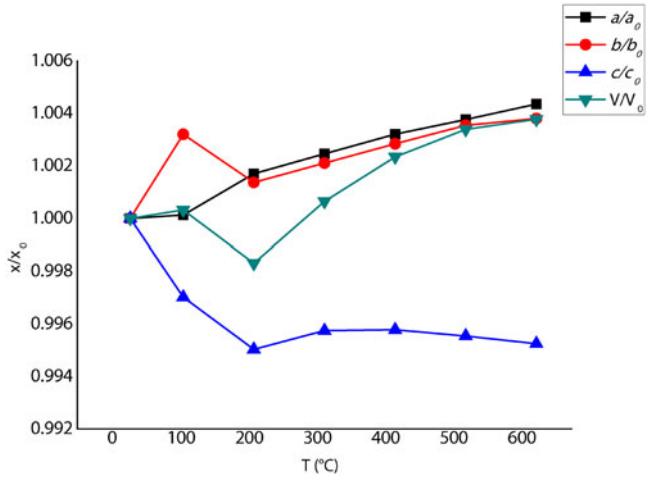

Figure 3. Normalised unit-cell parameters and volume of the studied fedorite *versus* temperature. a_0, b_0, c_0 and V_0 are cell parameters and volume at room temperature, respectively. The size of the symbols is larger than the associated esd's.

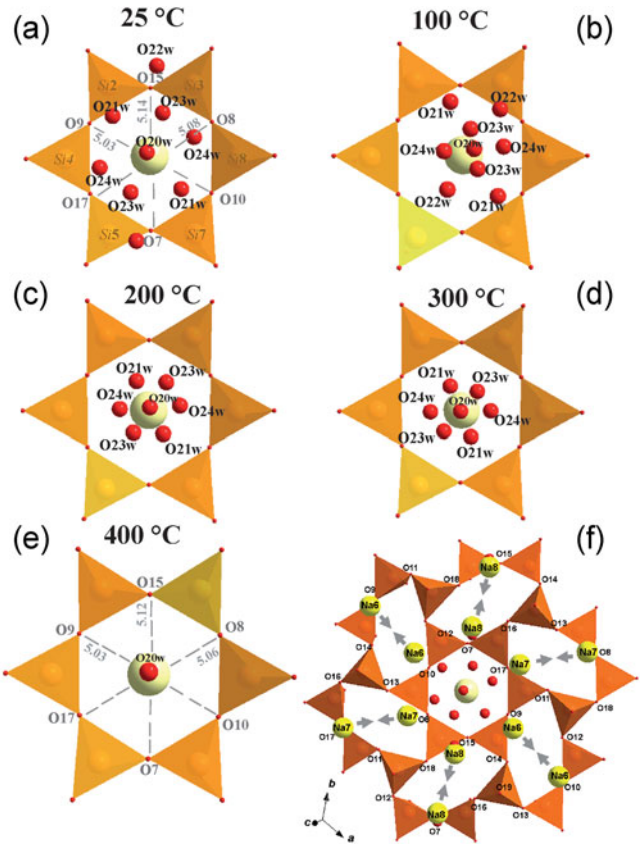

Figure 4. (a–e) Interlayer cavity of fedorite from refined structure in the RT–400°C temperature range with O–O internal diagonal distances in Å; (f) extended interlayer cavity view. Colours as reported in Fig. 2; grey arrows indicate the shift of Na cations with the temperature.

Crystal structure modifications and vibrational features upon heating

The thermal expansion of the fedorite structure proceeds from room temperature (RT) to 600°C without change in symmetry ($P\bar{1}$) and with a variation of the cell volume which encompasses the expansion along the *a* and *b* axis but also the decrease of the *c* cell dimension (Fig. 3; Table 2). With increasing temperature, the mineral progressively dehydrates up to 300°C when fedorite loses most of the H_2O as testified by the trend of the occupancies of O20w to O24w sites (Tables 3, 4, S2). In particular, the H_2O at O22w, which is very close to the interlayer cation at *Na*8 at RT, is lost after 100°C (Fig. 4). The H_2O at O21w, O23w and O24w positions, located in the *ab* plane, tend to shift toward the O20w site (Fig. 4a–e; Table 6). O20w is indeed the only occupied site at $T \geq 400$°C (Tables 3, 4, S2). Figure 5 shows that the total mean atomic number of the H_2O sites progressively decrease with temperature whereas the electron density of the O20w increases at $T > 300$°C as a consequence of the H_2O migration from the O21w, O23w and O24w sites towards O20w.

The dehydration process proceeds from RT up to 400°C causing the distortion of the hexagonal rings of downward-pointing tetrahedra as testified by the shortening of the O8–O17 and O7–O15 internal diagonal distances (Fig. 4a,e; Table 6). The cations in the *Na*5/*K* site shift along the *c* axis direction by moving away from the O20w and towards the F atoms, with a consequent remarkable lengthening of the *Na*/*K*–O20w distance that is balanced by the

https://doi.org/10.1180/mgm.2023.31 Published online by Cambridge University Press

Table 6. Selected anion–anion bond distances (Å) and *Si*1–O19–*Si*6 bond angles (°) derived from the structure refinement of the studied fedorite from 25 to 600°C.

	25°C	100°C	200°C	300°C	400°C	500°C	600°C
O20w–O21w	1.59(3)	1.63(5)	0.93(3)	0.88(4)	-	-	-
O20w–O22w	2.81(5)	1.50(4)	-	-	-	-	-
O20w–O23w	1.36(2)	0.62(5)	0.94(3)	0.84(4)	-	-	-
O20w–O24w	1.57(2)	0.94(2)	1.03(3)	0.98(4)	-	-	-
O20w–F	4.984(2)	4.965(2)	4.953(3)	4.967(2)	4.981(2)	4.986(2)	4.992(2)
O8–O17	5.077(2)	5.062(5)	5.053(2)	5.055(2)	5.064(2)	5.074(2)	5.080(2)
O7–O15	5.141(2)	5.143(5)	5.126(3)	5.121(3)	5.122(3)	5.129(3)	5.133(3)
O9–O10	5.031(2)	5.023(4)	5.031(3)	5.031(3)	5.030(3)	5.034(3)	5.039(3)
*Si*1–O19–*Si*6	175.94(9)	175.5(1)	175.2(9)	175.6(1)	175.5(1)	175.5(1)	175.4(1)

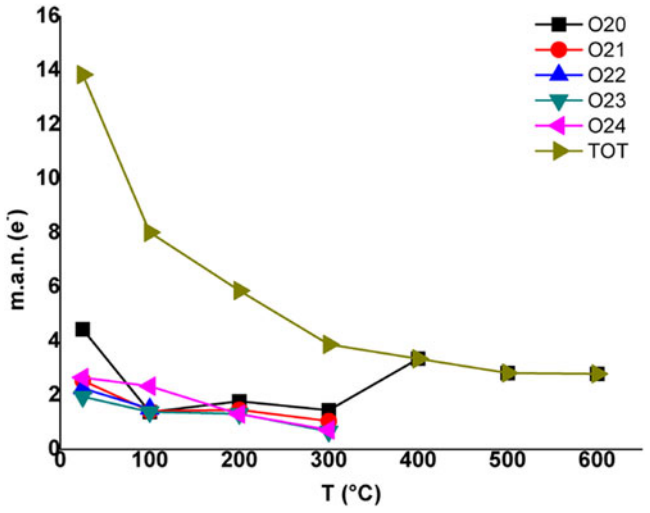

Figure 5. Mean atomic numbers (m.a.n., e^-) of H_2O *versus* temperature.

shortening of the *Na*/*K*–F distance (Fig. S4; Tables 5, S3). On the contrary, the cations at the *Na*6, *Na*7 and *Na*8 interlayer sites seem to move substantially in the *ab* plane, with their *z* coordinates almost unchanged during heating (Tables 3, 4, S2). In particular, they progressively increase their distance from O20w (Fig. S4). In addition, the cation at *Na*6 slightly moves away from the O10 atom and approaches O14; the cation at *Na*7 moves away from the O17 and shifts towards O11 and O13; the cation at *Na*8 moves from the O7 and O15 atoms towards the O16, O18 and O19 oxygens (Fig. S4, 4f). This also results in the shortening of the distances between equivalent Na cations (see the arrows directions in Fig. 4f). A slight variation of the effective coordination number (ECoN parameter, from 9.86 to 7.90) of the cation at the *Na*5 site from RT to 400°C has been observed.

Finally, structure refinements of the partially dehydrated fedorite (from 400 to 600°C) show that no significant geometric modifications of the tetrahedral and octahedral sheets were induced by the heating process, as quite similar values were obtained for tetrahedral and octahedral mean distances and geometrical parameters (Tables 5, S3).

The infrared spectra of the fedorite sample annealed at different temperatures (from 25 to 700°C) are given in Fig. 6. The group of peaks observed at 1119, 1030, 790, 618 cm^{-1} may be assigned to the asymmetric and symmetric Si–O stretching modes of the SiO_4 tetrahedra.

The peak at 618 cm^{-1} in the sample studied is slightly shifted in comparison with the same peak in Gav-43 and Irk-53 samples (615 cm^{-1}; Kaneva *et al.* 2020a). The energy of bending vibrations of SiO_4 at 615 cm^{-1} slightly increased in the sample studied, which contains a greater amount of H_2O. The same behaviour of SiO_4 bending vibrations has been observed in elpidite samples in Bogdanov *et al.* (2021).

Intensities of H–O–H asymmetric and symmetric stretching vibrations in the region 3000–3700 cm^{-1} (inset in Fig. 6) and bending ones at 1627 cm^{-1} decreased during annealing. This indicates that the fedorite sample lost H_2O. In addition, the peak at 790 cm^{-1} in the pristine sample shifts to 796 cm^{-1} in the sample annealed at 700°C, when fedorite lost almost all H_2O. This could be due to a slight change in Si–O–Si angles during annealing (Shendrik *et al.*, 2021).

The 3000–3700 cm^{-1} region of the absorption spectrum related to OH-stretching vibrations has a complicated shape (Fig. 6). Six peaks, at 3177, 3429, 3549, 3588, 3635 and 3656 cm^{-1}, can be seen clearly for the sample at room temperature. Such peaks are similar to those found in the Irk-53 sample (Kaneva *et al.* 2020b). Three groups of peaks can be distinguished on the basis of the behaviour during heating (Figs 6, 7). Group 1 includes the 3588 and 3656 cm^{-1} peaks. The intensity of these peaks decreases as the temperature increases and becomes negligible at temperatures >327°C (Fig. 7). Group 2 includes the 3177, 3429, 3549 and 3635 cm^{-1} peaks. Their intensity gradually decreases upon annealing and becomes negligible above 627°C (Fig. 7). Group 3 includes 3576 and 3650 cm^{-1} peaks. The latter start to be observed at >150°C and show the maximum intensity at 350°C (Fig. 7). Further annealing at higher temperatures leads to a decrease in their intensity. Peaks belonging to Group 1 and 3 are sharp and may be attributed to OH-anions in different positions or to O–H stretching vibrations (hydrogen bonds of medium strengths). Group 2 bands may be attributed to H_2O with a strong hydrogen bond. The trends of the band intensities (Fig. 7) in the FTIR spectra could be explained by taking into account the results of the HT-SXRD structure refinements. Specifically, the quick decrease of the intensity observed for Group 1 agrees with the reduction of the total H_2O mean atomic numbers up to 300°C (Fig. 5). The intensity variation of Group 3 seems to describe the migration of H_2O at $T \geq 100$°C (Fig. 4). Finally, the gradual decrease of the band intensity of Group 2 represents the evolution of the dehydration process very well, affecting the fedorite up to $T \approx 600$°C, as described above.

Conclusions

For the first time a combination of thermal, *in situ* HT-SCXRD and *ex situ* HT-FTIR analyses has allowed the thermal behaviour, and specifically, the dehydration process of a fedorite sample from Murun massif to be examined in detail.

https://doi.org/10.1180/mgm.2023.31 Published online by Cambridge University Press

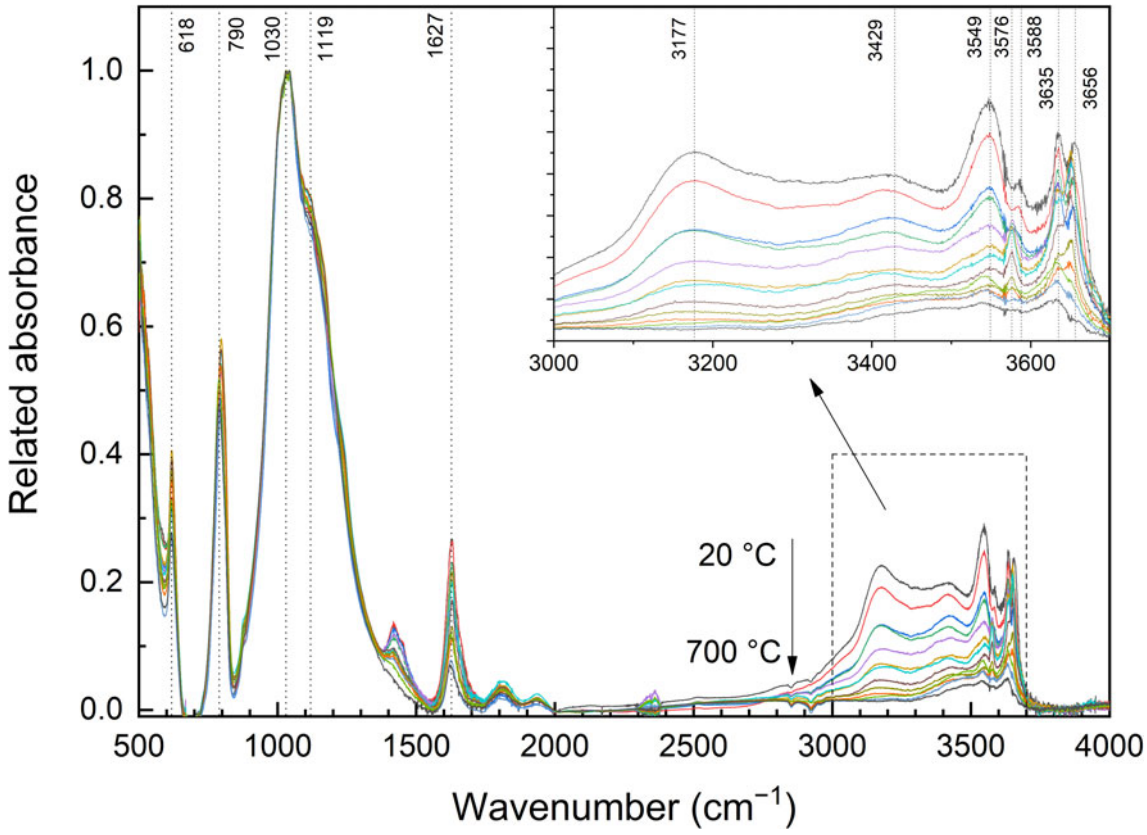

Figure 6. IR absorption spectra of fedorite annealed at different temperatures. Inset shows the region of O–H stretching vibrations in detail.

The mineral contains ~3 H_2O gpfu, which occupy five different crystallographic sites (O20w to O24w) in the structure refined at room temperature, whereas at 600°C only O20w is occupied. Fedorite underwent thermal expansion in the whole temperature range (25–600°C) explored by XRD with a preferential dilatation along the *a* and *b* axes while a decrement in the *c* cell parameter was a consequence of the dehydration process. It is interesting that the dehydration of fedorite results in an expansion of the unit-cell volume (~0.4%). Other minerals (i.e., layered minerals) are usually subjected to a remarkable volume contraction following dehydration. Volume contraction in fedorite upon dehydration is actually limited by the topology of the $[Si_{16}O_{38}]^{12-}$ unit that is described by Hawthorne *et al.* (2019). As shown in Fig. 2, the single tetrahedral sheets are interconnected by *Si*1 and *Si*6 tetrahedra that intrude the interlayer space thus forming the 'rigid skeleton' of the cavity where alkaline cations and H_2O are hosted. As the temperature increases from 25 to 600°C, *Si*1 and *Si*6 tetrahedra do not vary in terms of individual and average bond distances (see Table 5, S3) whereas the *Si*1–O19–*Si*6 angles show a variation (from 175.94(9) to 175.4(1)°, see Table 6) that, although small, has the same trend as the *c*-cell parameter (Fig. 3). This could explain why the cavity cannot shrink significantly after losing the H_2O.

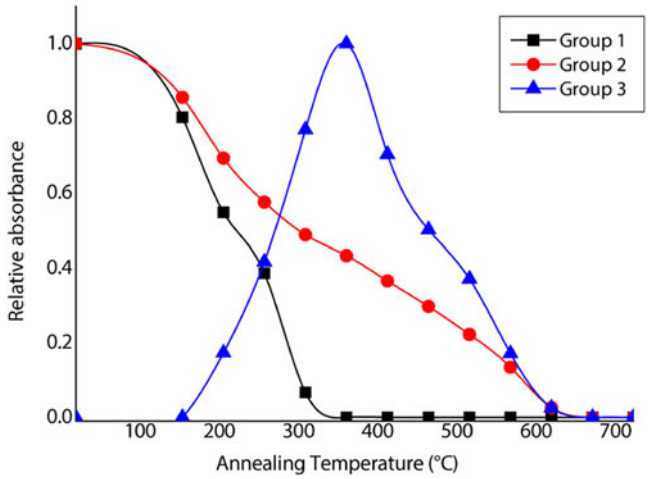

Figure 7. Temperature dependence as a function of the relative intensity of IR absorption of different OH-stretching vibration groups for the annealed fedorite sample.

All the analytical techniques used testified for a continuous dehydration reaction up to $T \approx 600$°C, whereas the complete loss of H_2O at 650–700°C was highlighted by the TG curve. The combination of the XRD and FTIR results allowed us to examine the features of the partially dehydrated structures in detail. In particular, one H_2O (at the O22w site) leaves the interlayer site early, whereas a reduction in the amount of the remaining H_2O proceeds rapidly up to $T \approx 300$°C. This process is accompanied by the migration of the H_2O at O21w–O24w sites towards the O20w position and by the shortening of Na–Na distances for the cations at *Na*6 to *Na*8 sites. The release of the F atoms occurred above 700°C (TG curve) whereas the breakdown of the structure at ~1000°C was demonstrated by the DTA curve.

Finally, the present work reports the thermal behaviour of a fedorite sample with $Na^+ > K^+$. Note that this composition is

https://doi.org/10.1180/mgm.2023.31 Published online by Cambridge University Press

different from that of fedorite as defined in the IMA–CNMNC *List of Mineral Names* (Pasero, 2023), however it is similar to that reported in previous studies (specifically Joswig *et al.*, 1988 and Mitchell and Burns, 2001). Although a different K/Na ratio could affect the dehydration process, the overall thermal behaviour of the mineral is not expected to vary significantly because of the bond topology. However, further studies on samples with different compositions have to be carried out to understand how the crystal chemistry of fedorite affects its structural modification at high temperature.

Acknowledgements. Vasiliy Sychev is thanked for providing the samples for the study; Mikhail Mitichkin for sample polishing and thin-section preparation; Prof. Stefano Poli and Dr. A. Risplendente for the facilities at the Electron Microprobe Laboratory of the Dipartimento di Scienze della Terra, Università di Milano; Prof. D. Malferrari for performing thermal analysis. The IR spectroscopic and optical petrographic study were carried out using facilities of the Vinogradov Institute of Geochemistry SB RAS (Irkutsk). The optical petrographic study was performed by the governmental assignment in terms of Project № 0284-2021-0008. This work was supported by a M. Lacalamita grant (SIMP 2020 Research Grant in Crystal-chemistry, in memory of Prof. Fiorenzo Mazzi). Three anonymous referees are gratefully acknowledged for their insightful suggestions.

Supplementary material. The supplementary material for this article can be found at https://doi.org/10.1180/mgm.2023.31.

Competing interests. The authors declare none.

References

Betteridge P.W., Carruthers J.R., Cooper R.I., Prout K. and Watkin D.J. (2003) Crystals version 12: software for guided crystal structure analysis. *Journal of Applied Crystallography*, **36**, 1487.

Blackburn W.H. and Dennen W.H. (1997) *Encyclopedia of Mineral Names*. The Canadian Mineralogist Special Publication 1. Mineralogical Association of Canada, Ottawa, Canada, 360 pp.

Bogdanov A., Kaneva E. and Shendrik R. (2021) New insights into the crystal chemistry of elpidite, $Na_2Zr[Si_6O_{15}]\cdot 3H_2O$ and $(Na_{1+Y}Ca_x\square_{1-X-Y})_{\Sigma=2}Zr[Si_6O_{15}]\cdot(3-X)H_2O$, and ab initio modeling of IR spectra. *Materials*, **14**, 2160.

Bonaccorsi E. and Merlino S. (2005) Modular microporous minerals: Cancrinite–davine group and C-S-H phases. Pp. 241–290 in: *Micro- and Mesoporous Mineral Phases* (G. Ferraris and S. Merlino, editors). Reviews in Mineralogy and Geochemistry, **57**. Mineralogical Society of America and the Geochemical Society, Chantilly, Virginia, USA.

Borovikov A.A., Vladykin N.V., Tretiakova I.G. and Dokuchits E.Yu (2018) Physicochemical conditions of formation of hydrothermal titanium mineralization on the Murunskiy alkaline massif, western Aldan (Russia). *Ore Geology Reviews*, **95**, 1066–1075.

Breese N.E. and O'Keeffe M. (1991) Bond-valence parameters for solids. *Acta Crystallographica*, **B47**, 192–197.

Brown I.D. (2006) *The Chemical Bond in Inorganic Chemistry: The Bond Valence Model*. Oxford University Press, Oxford, 278 pp.

Brown I.D. and Altermatt D. (1985) Bond-valence parameters obtained from a systematic analysis of the Inorganic Crystal Structure Database. *Acta Crystallographica*, **B41**, 244–247.

Bruker (2007) *SAINT*. Bruker AXS Inc., Madison, Wisconsin, USA.

Bruker (2009) *SADABS*. Bruker AXS Inc., Madison, Wisconsin, USA.

Comboni D., Lotti P., Gatta G.D., Lacalamita M., Mesto E., Merlini M. and Hanfland M. (2019) Armstrongite at non-ambient conditions: An *in-situ* high-pressure single-crystal X-ray diffraction study. *Microporous and Mesoporous Materials*, **274**, 171–175.

Ferraris G. (1997) Polysomatism as a tool for correlating properties and structure. Pp. 275–295 in: *Modular Aspects of Minerals* (S. Merlino, editor). European Mineralogical Union, volume 1.

Ferraris G. and Gula A. (2005) Polysomatic aspects of microporous minerals – Heterophyllosilicates, palysepioles and rhodesite-related structures. Pp. 69–104 in: *Micro- and Mesoporous Mineral Phases* (G. Ferraris and S. Merlino, editors). Reviews in Mineralogy and Geochemistry, **57**. Mineralogical Society of America and the Geochemical Society, Chantilly, Virginia, USA.

Hawthorne F.C., Uvarova Y.A. and Sokolova E. (2019) A structure hierarchy for silicate minerals: sheet silicates. *Mineralogical Magazine*, **83**, 3–55.

Ilinca G. (2022) Charge distribution and bond valence sum analysis of sulfosalts – the ECoN21 Computer Program. *Minerals*, **12**, 924.

Ivanov A.V., Vladykin N.V., Demonterova E.I., Gorovoy V.A. and Dokuchits E.Y. (2018) $^{40}Ar/^{39}Ar$ geochronology of the Malyy (Little) Murun massif, Aldan shield of the Siberian craton: A simple story for an intricate igneous complex. *Minerals*, **8**, 602.

Joswig W., Drits V.A. and Sokolova G.V. (1988) Refinement of the structure of fedorite. *Soviet Physics-Crystallography*, **33**, 763–765.

Kaneva E. and Shendrik R. (2022) Tinaksite and tokkoite: x-ray powder diffraction, optical and vibrational properties. *Crystals*, **12**, 377.

Kaneva E., Lacalamita M., Mesto E., Schingaro E., Scordari F. and Vladykin N. (2014) Structure and modeling of disorder in miserite from the Murun (Russia) and Dara-i-Pioz (Tajikistan) massifs. *Physics and Chemistry of Minerals*, **41**, 49–63.

Kaneva E.V., Vladykin N.V., Mesto E., Lacalamita M., Scordari F. and Schingaro E. (2018) Refinement of the crystal structure of vlasovite from Burpala Massif (Russia). *Crystallography Reports*, **63**, 1092–1098.

Kaneva E.V., Shendrik R.Yu., Radomskaya T.A. and Suvorova L.F. (2020a) Fedorite from Murun alkaline complex (Russia): spectroscopy and crystal chemical features. *Minerals*, **10**, 702.

Kaneva E., Shendrik R., Mesto E., Bogdanov A. and Vladykin N. (2020b) Spectroscopy and crystal chemical properties of $NaCa_2[Si_4O_{10}]F$ natural agrellite with tubular structure. *Chemical Physics Letters*, **738**, 136868.

Kaneva E., Bogdanov A. and Shendrik R. (2020c) Structural and vibrational properties of agrellite. *Scientific Reports*, **10**, 15569.

Kaneva E.V., Shendrik R.Y., Vladykin N.V., Radomskaya T.A. (2021) Crystal-chemical features of rare and complex silicates from charoite rocks of the Malyy Murun Volcano-Plutonic Alkaline Complex. Pp. 115–129 in: *Alkaline Rocks, Kimberlites and Carbonatites: Geochemistry and Genesis*. Proceedings of the XV International Seminar "Deep-seated magmatism, its sources and plumes", 1-7 September 2019, Russia, Saki. Springer Proceedings in Earth and Environmental Sciences.

Kaneva E., Radomskaya T., Shendrik R. (2022) Fluorcarletonite – a new blue gem material. *Journal of Gemmology*, **38**, 376–385.

Kaneva E., Bogdanov A., Radomskaya T., Belozerova O. and Shendrik R. (2023a) Crystal-chemical characterization and spectroscopy of fluorcarletonite and carletonite. *Mineralogical Magazine*, **87**, 356–368, https://doi.org/10.1180/mgm.2023.15.

Kaneva E., Radomskaya T., Belozerova O. and Shendrik R. (2023b) Crystal chemistry of turkestanite (Dara-i-Pioz massif, Tajikistan). *Mineralogical Magazine*, **87**, 252–261 https://doi.org/10.1180/mgm.2023.3.

Konev A.A., Vorobjov E.I. and Bulach, A. (1993) Charoit – der Schmuckstein aus Sibirien und seine seltenen Begleitminerale. *Lapis*, **18**, 13–20.

Konev A.A., Vorob'ev E.I. and Lazebnik K.A. (1996) *Mineralogy of the Murunsky Alkaline Massif*. SIC UIGGM, Publishing House of SB RAS, Novosibirsk, 221 pp. [in Russian].

Kukharenko A.A., Orlova M.P., Bulakh A.G., Bagdasarov E.A., Rimskaya-Korsakova O.M., Nefedov E.I., Il'inskii G.A., Sergeev A.S. and Abakumova N.B. (1965) *Caledonian Complex of Ultrabasic, Alkaline Rocks and Carbonatites of the Kola Peninsula and North Karelia*. Nedra, Moscow, Russia, 772 pp.

Lacalamita M. (2018) Micro-FTIR and EPMA characterisation of charoite from Murun Massif (Russia). *Journal of Spectroscopy*, **2018**, 9293637.

Lacalamita M., Mesto E., Kaneva E., Scordari F., Pedrazzi G., Vladykin N. and Schingaro E. (2017) Structure refinement and crystal chemistry of tokkoite and tinaksite from the Murun massif (Russia). *Mineralogical Magazine*, **81**, 251–272.

Lacalamita M., Cametti G., Mesto E. and Schingaro E. (2019) Armstrongite at non ambient conditions: An in-situ high temperature single crystal X-ray diffraction study. *Microporous and Mesoporous Materials*, **275**, 180–190.

Mesto E., Kaneva E., Schingaro E., Vladykin N., Lacalamita M., Scordari F. (2014) Armstrongite from Khan Bogdo (Mongolia): Crystal structure

determination and implications for zeolite-like cation exchange properties. *American Mineralogist*, **99**, 2424–2432.

Mitchell R.H. and Burns P.C. (2001) The structure of fedorite: A re-appraisal. *The Canadian Mineralogist*, **39**, 769–777.

Pasero M (2023) *The New IMA List of Minerals*. International Mineralogical Association. Commission on new minerals, nomenclature and classification (IMA-CNMNC). http://cnmnc.units.it/

Pouchou J.L. and Pichoir F. (1985) "PAP" φ(ρZ) procedure for improved quantitative micro analysis. Pp 104–106 in: *Microbeam Analysis* (J.T. Armstrong, editor). San Francisco Press Inc., San Francisco.

Rastsvetaeva R.K. and Aksenov S.M. (2011) Crystal chemistry of silicates with three-layer *TOT* and *HOH* modules of layered, chainlike, and mixed types. *Crystallography Reports*, **56**, 910–934.

Sapozhnikov A.N., Tauson V.L., Lipko S.V., Shendrik R.Yu., Levitskii V.I., Suvorova L.F., Chukanov N.V. and Vigasina M.F. (2021) On the crystal chemistry of sulfur-rich lazurite, ideally $Na_7Ca(Al_6Si_6O_{24})(SO_4)(S_3)^{-}\cdot nH_2O$. *American Mineralogist*, **106**, 226–234.

Schingaro E., Mesto E., Lacalamita M., Scordari F., Kaneva E. and Vladykin F.N. (2017) Single-crystal X-ray diffraction, EMPA, FTIR and X-ray photoelectron spectroscopy study of narsarsukite from Murun Massif, Russia. *Mineralogical Magazine*, **81**, 339–354.

Schingaro E., Lacalamita M., Mesto E. and Della Ventura G.C. (2018) Thermal stability and dehydration of armstrongite, a microporous zirconium silicate. *Microporous and Mesoporous Materials*, **272**, 137–142.

Shendrik R., Kaneva E., Radomskaya T., Sharygin I. and Marfin A. (2021) Relationships between the structural, vibrational, and optical properties of microporous cancrinite. *Crystals*, **11**, 280.

Sokolova G.V., Kashaev A.A., Drits V.A. and Ilyukhin V.V. (1983) The crystal structure of fedorite. *Soviet Physics-Crystallography*, **28**, 170–172.

Vladykin N.V. (2009) Potassium alkaline lamproite-carbonatite complexes: Petrology, genesis, and ore reserves. *Russian Geology Geophysics*, **50**, 1119–1128.

Vladykin N.V., Borokovikov A.A., Dokuchits E.Yu. and Thomas V.G. (2018) Genesis of charoite rocks in the Murun massif, Aldan Shield, Russia. *Geochemistry International*, **56**, 1135–1147.

Zema M., Ventruti G., Tarantino S. and Micelli C. (2022) A new thermal and atmospheric conditioning device for in situ single-crystal diffraction is up and running. *Geosciences for a Sustainable Future, Torino, Italy*, S18–21 [abstracts].

https://doi.org/10.1180/mgm.2023.31 Published online by Cambridge University Press